J|A|C|S ARTICLES

Published on Web 08/06/2010

Probing the Rate of Hole Transfer in Oxidized Porphyrin Dyads Using Thallium Hyperfine Clocks

James R. Diers,[†] Masahiko Taniguchi,[‡] Dewey Holten,*[,§] Jonathan S. Lindsey,*[,‡] and David F. Bocian*[,†]

Departments of Chemistry, University of California, Riverside, California 92521-0403, North Carolina State University, Raleigh, North Carolina 27695-8204, and Washington University, St. Louis, Missouri 63130-4889

Received June 10, 2010; E-mail: david.bocian@ucr.edu; jlindsey@ncsu.edu; holten@wustl.edu

Abstract: Understanding hole/electron-transfer processes among interacting constituents of multicomponent molecular architectures is central to the fields of artificial photosynthesis and molecular electronics. One strategy for examining ground-state hole/electron transfer in oxidized tetrapyrrolic arrays entails analysis of the hyperfine interactions observed in the electron paramagnetic resonance (EPR) spectrum of the π-cation radical. Herein, it is demonstrated that ^{203}Tl/^{205}Tl hyperfine "clocks" are greatly superior to those provided by ^{1}H, ^{14}N, or ^{13}C owing to the fact that the ^{203}Tl/^{205}Tl hyperfine couplings are much larger (15−25 G) than those of the ^{1}H, ^{14}N, or ^{13}C nuclei (1−6 G). The large ^{203}Tl/^{205}Tl hyperfine interactions permit accurate simulations of the EPR spectra and the extraction of specific rates of hole/electron transfer. The ^{203}Tl/^{205}Tl hyperfine clock strategy is applied to a series of seven porphyrin dyads. All of the dyads are joined at a meso position of the porphyrin macrocycle via linkers of a range of lengths and composition (diphenylethyne, diphenylbutadiyne, and (*p*-phenylene)$_n$, where $n = 1-4$); substituents such as mesityl at the nonlinking meso positions are employed to provide organic solubility. The hole/electron-transfer time constants are in the hundreds of picoseconds to sub-10 ns regime, depending on the specific porphyrin and/or linker. Density functional theory calculations on the constituents of the dyads are consistent with the view that the relative energies of the porphyrin versus linker highest occupied molecular orbitals strongly influence the hole/electron-transfer rates. Variable-temperature EPR studies further demonstrate that the hole/electron-transfer process is at best weakly activated (12−15 kJ mol^{-1}) at room temperature and somewhat below. At lower temperatures, the process is essentially activationless. The weak activation is attributed to restricted torsional motions of the phenyl rings of the linker. Collectively, the studies provide the physical basis for the rational design of multicomponent architectures for efficient hole/electron transfer.

1. Introduction

Understanding electronic communication among interacting chromophores is essential for the rational design of molecular architectures for artificial photosynthetic light-harvesting and energy conversion. Porphyrinic macrocycles have been widely employed in the construction of synthetic light-harvesting arrays owing to their attractive and versatile physical properties and amenability to synthetic control.[1−16] An effective light-harvesting array absorbs intensely and transfers the resulting electronic excited-state energy to a specific site with high efficiency. Conversion of the harvested excited-state energy to electrical energy then requires efficient electron injection into the anode, followed by efficient ground-state hole migration away from the anode, thereby preventing charge recombination. Accordingly, understanding hole mobility in prototypical light-harvesting and charge-separation systems is of fundamental interest.

Over the past decade or more, our groups have investigated ground-state hole/electron transfer in oxidized porphyrinic arrays using electron paramagnetic resonance (EPR) spectroscopy.[13] More recently, we have developed transient absorption spec-

[†] University of California, Riverside.
[‡] North Carolina State University.
[§] Washington University.

(1) Maretina, I. A. *Russ. J. Gen. Chem.* **2009**, *79*, 1544–1581.
(2) Aratani, N.; Kim, D.; Osuka, A. *Acc. Chem. Res.* **2009**, *42*, 1922–1934.
(3) Flamigni, L. *J. Photochem. Photobiol. C: Photochem. Rev.* **2007**, *8*, 191–210.
(4) Nakamura, Y.; Aratani, N.; Osuka, A. *Chem. Soc. Rev.* **2007**, *36*, 831–845.
(5) Lo, P.-C.; Leng, X.; Ng, D. K. P. *Coord. Chem. Rev.* **2007**, *251*, 2334–2353.
(6) Kobuke, Y. *Struct. Bonding (Berlin)* **2006**, *121*, 49–104.
(7) Iengo, E.; Scandola, F.; Alessio, E. *Struct. Bonding (Berlin)* **2006**, *121*, 105–143.
(8) Balaban, T. S. *Acc. Chem. Res.* **2005**, *38*, 612–623.
(9) Balaban, T. S.; Tamiaki, H.; Holzwarth, A. R. *Top. Curr. Chem.* **2005**, *258*, 1–38.
(10) Imahori, H. *J. Phys. Chem. B* **2004**, *108*, 6130–6143.
(11) Harvey, P. D. In *The Porphyrin Handbook*; Kadish, K. M., Smith, K. M., Guilard, R., Eds.; Academic Press: San Diego, 2003; Vol. 18, pp 63−250.
(12) Aratani, N.; Osuka, A. *Chem. Record* **2003**, *3*, 225–234.
(13) Holten, D.; Bocian, D. F.; Lindsey, J. S. *Acc. Chem. Res.* **2002**, *35*, 57–69.
(14) Aratani, N.; Osuka, A. *Macromol. Rapid Commun.* **2001**, *22*, 725–740.
(15) Burrell, A. K.; Officer, D. L.; Plieger, P. G.; Reid, D. C. W. *Chem. Rev.* **2001**, *101*, 2751–2796.
(16) Gust, D.; Moore, T. A.; Moore, A. L. *Acc. Chem. Res.* **2001**, *34*, 40–48.

troscopic approaches for determining the rates of ground-state hole/electron-transfer processes.[17] In parallel with the development of the transient optical methods, we have continued our exploration of alternative EPR methods for probing ground-state hole/electron transfer.

The use of EPR techniques to examine ground-state hole/electron transfer relies on the measurement of the modulation of hyperfine interactions via the hole/electron-transfer process. In this regard, our early EPR studies utilized porphyrinic arrays of natural isotopic composition, thereby restricting the studies to measurements of ^{14}N and/or ^{1}H interactions.[13,18−20] The reliance on ^{14}N and ^{1}H hyperfine interactions is a severe constraint because these couplings are relatively small (<3 G) in porphyrin π-cation radicals.[21] As a consequence, the exact rates of hole/electron transfer could not be extracted from the data; it could only be determined whether the process is fast or slow on the EPR time scale (dictated by the magnitude of the hyperfine interactions). More recently, we have attempted to mitigate the limitations of the EPR method by embarking on molecular design strategies that entail introduction of a ^{13}C label at specific sites in the porphyrin macrocycle where there is substantial hole/electron density in the relevant frontier (highest occupied) molecular orbital (HOMO).[22,23] The incorporation of ^{13}C labels has two advantages: (1) The ^{13}C hyperfine interactions in porphyrin π-cation radicals are typically larger than those of ^{14}N or ^{1}H.[21,24] (2) The introduction of an additional hyperfine coupling affords more accurate simulations of the EPR spectra.

Although a variety of tetrapyrroles containing site-specific ^{13}C labels have been synthesized,[22,23,25] an alternative hyperfine clock is desirable to further enhance the robustness of the EPR spectral simulations of the π-cation radicals of arrays and to extract specific rates of hole/electron transfer. Inspection of the characteristics of the nuclei across the periodic table reveals that there are relatively few options for alternative hyperfine clocks—thallium is by far the best choice. ^{203}Tl and ^{205}Tl occur naturally in a 30/70 isotopic ratio; both are $I = 1/2$ nuclei with nearly equal magnetogyric ratios (within 1%).[26] The small difference in the magnetogyric ratios suggests that there should be no need for preparation of isotopically pure complexes because the hyperfine splittings of the two isotopes of thallium should not be distinguishable. Another key feature of the thallium nuclei is that the magnetogyric ratios are extremely large, ~60% of that of ^{1}H. Accordingly, very small spin density on the thallium metal center should yield significant hyperfine splittings. In this regard, early EPR studies of ^{205}Tl porphyrin π-cation radicals revealed hyperfine splittings as large as 60 G.[27] In the thallium porphyrins, the metal is trivalent, contains an apical counterion, and does not participate in the redox process. The magnitude of the ^{205}Tl hyperfine splittings can be varied depending on the nature of the counterion to the Tl(III) ion.[27] Regardless, the ^{205}Tl hyperfine splittings are much larger (10−20-fold) than those for ^{13}C, ^{14}N, or ^{1}H.[21−25]

The above-noted attributes of thallium nuclei along with the observations reported in the early EPR studies of monomeric ^{205}Tl porphyrin π-cation radicals motivated us to synthesize and characterize a series of thallium porphyrin dyads.[28] The structures of the dyads are shown in Chart 1 and have the following features. (1) All of the dyads are linked at the meso position of the porphyrin ring. (2) Two dyads are linked via a diphenylethyne group: one has nonlinking meso mesityl substituents, **TlTl-Mes-PEP**, and the other has nonlinking meso-branched tridecyl ("swallowtail") substituents, **TlTl-SW-PEP**. (3) Another dyad is linked via a diphenylbutadiyne and contains nonlinking meso mesityl substituents, **TlTl-Mes-PEEP**. (4) Four dyads are linked via oligo(*p*-phenylene) units wherein the number of phenylene rings varies from one to four; the nonlinking meso substituents are mesityls, **TlTl-Mes-Φ_n** (n = 1−4). In addition to the thallium porphyrin dyads, two benchmark monomeric thallium porphyrins were prepared; the structures of these monomers are shown in Chart 2. These porphyrins both contain a phenylethyne group at one meso position: one has mesityl substituents, **Tl-Mes-PE**, and the other has swallowtail substituents, **Tl-SW-PE**, at the other meso positions.

The rationale for the choice of the particular thallium porphyrin dyads was as follows.

(1) Comparison of the trimesityl- versus tri-swallowtail-substituted dyads probes the effects of altering the relative energies of the HOMO of the porphyrin versus the diphenylethyne linker that is common to both **TlTl-SW-PEP** and **TlTl-Mes-PEP**. The difference in HOMO energy of the mesityl- versus swallowtail-substituted porphyrins is reflected in the oxidation potential, which is known to be ~150 mV lower for zinc-chelated tetra-swallowtail versus tetramesityl porphyrins.[29] As an accompaniment to the studies of the two thallium porphyrin dyads, the zinc analogue of the swallowtail dyad, **Zn*Zn-SW-PEP**, and the benchmark monomer, **Zn*SW-PEP**,[22] were also examined. These compounds contain a single ^{13}C label at the linking meso position, as shown in Chart 3. [In the case of the dyad, only one of the two porphyrins contains the ^{13}C label.] The motivation for comparing the zinc and thallium analogues was the anticipation that the redox potential, and hence the porphyrin HOMO energy, would differ in the zinc versus thallium species. The **TlTl-Mes-PEEP** dyad was examined as an additional accompaniment to the studies of the diphenylethyne-linked dyads.

(2) Comparison of the oligo(*p*-phenylene)-linked dyads probes the effects of systematically increasing the length of the linker

(17) (a) Song, H.-E.; Taniguchi, M.; Diers, J. R.; Kirmaier, C.; Bocian, D. F.; Lindsey, J. S.; Holten, D. *J. Phys. Chem. B* **2009**, *113*, 16483–16493. (b) Song, H.-E.; Kirmaier, C.; Taniguchi, M.; Diers, J. R.; Bocian, D. F.; Lindsey, J. S.; Holten, D. *J. Am. Chem. Soc.* **2008**, *130*, 15636–15648. (c) Song, H.-E.; Taniguchi, M.; Kirmaier, C.; Bocian, D. F.; Lindsey, J. S.; Holten, D. *Photochem. Photobiol.* **2009**, *85*, 693–704.
(18) Seth, J.; Palaniappan, V.; Johnson, T. E.; Prathapan, S.; Lindsey, J. S.; Bocian, D. F. *J. Am. Chem. Soc.* **1994**, *116*, 10578–10592.
(19) Seth, J.; Palaniappan, V.; Wagner, R. W.; Johnson, T. E.; Lindsey, J. S.; Bocian, D. F. *J. Am. Chem. Soc.* **1996**, *118*, 11194–11207.
(20) Yang, S. I.; Lammi, R. K.; Seth, J.; Riggs, J. A.; Arai, T.; Kim, D.; Bocian, D. F.; Holten, D.; Lindsey, J. S. *J. Phys. Chem. B* **1998**, *102*, 9426–9436.
(21) Fajer, J.; Davis, M. S. In *The Porphyrins*; Dolphin, D., Ed.; Academic Press: New York, 1979; Vol. 4, pp 197−256.
(22) Thamyongkit, P.; Muresan, A. Z.; Diers, J. R.; Holten, D.; Bocian, D. F.; Lindsey, J. S. *J. Org. Chem.* **2007**, *72*, 5207–5217.
(23) Muresan, A. Z.; Thamyongkit, P.; Diers, J. R.; Holten, D.; Lindsey, J. S.; Bocian, D. F. *J. Org. Chem.* **2008**, *73*, 6947–6959.
(24) Atamian, M.; Wagner, R. W.; Lindsey, J. S.; Bocian, D. F. *Inorg. Chem.* **1988**, *27*, 1510–1512.
(25) Nieves-Bernier, E. J.; Diers, J. R.; Taniguchi, M.; Holten, D.; Bocian, D. F.; Lindsey, J. S. *J. Org. Chem.* **2010**, *75*, 3193–3202.
(26) NMR Properties of Selected Isotopes. *Bruker Almanac 2010*; Bruker AXS Inc.: Madison, WI, 2010; http://www.bruker.com/fileadmin/be_user/news/Almanac/Almanac2010.pdf (accession date, 05/18/2010).
(27) Mengersen, C.; Subramaniam, J.; Fuhrhop, J. H.; Smith, K. M. *Z. Naturforsch.* **1974**, *29a*, 1827–1833.
(28) Taniguchi, M.; Lindsey, J. S. *Tetrahedron* **2010**, *66*, 5549–5565.
(29) Thamyongkit, P.; Speckbacher, M.; Diers, J. R.; Kee, H.-L.; Kirmaier, C.; Holten, D.; Bocian, D. F.; Lindsey, J. S. *J. Org. Chem.* **2004**, *69*, 3700–3710.

Chart 1

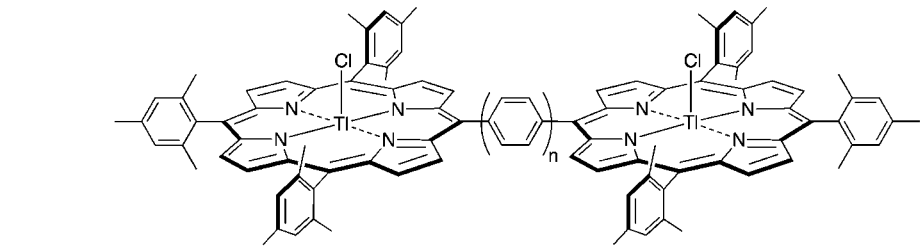

TITI-Mes-Φ_1 $n = 1$
TITI-Mes-Φ_2 $n = 2$
TITI-Mes-Φ_3 $n = 3$
TITI-Mes-Φ_4 $n = 4$

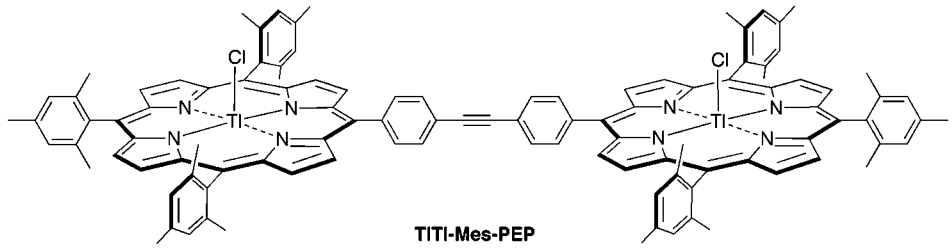

TITI-Mes-PEP

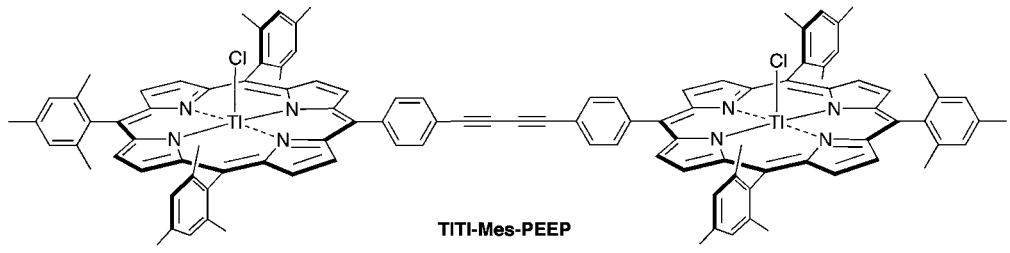

TITI-Mes-PEEP

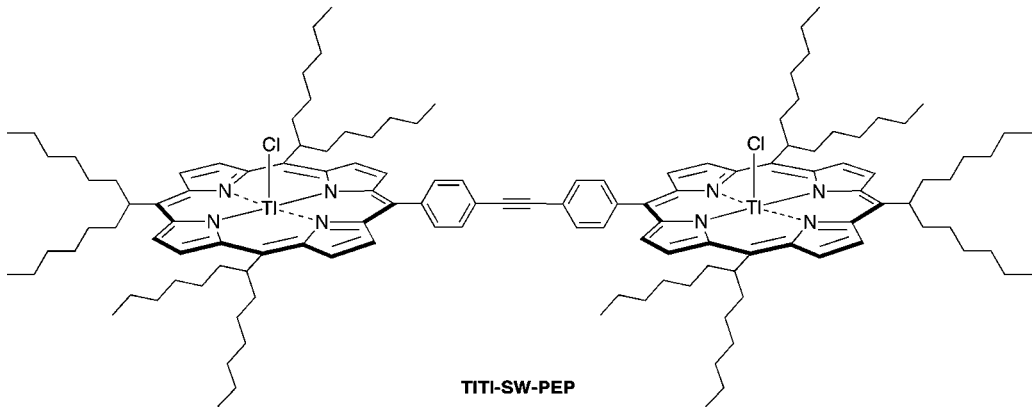

TITI-SW-PEP

that joins the trimesityl-substituted porphyrins that are common to all four dyads. The change in number of phenyl rings in the linker was also anticipated to result in a change in the relative energies of the linker versus porphyrin HOMOs.

Herein, we report EPR studies on the mono-π-cation radicals of the various porphyrins shown in Chart 1−3. Simulations of the spectra of the π-cation radicals of the dyads are performed to extract the specific hole/electron-transfer rates. Variable-temperature EPR studies are also conducted to obtain the activation energies for hole/electron transfer. The spectroscopic studies are accompanied by density functional theory (DFT) calculations on the various constituents of the dyads that are aimed at estimating the relative energies of the porphyrin and linker HOMOs. Collectively, the studies provide new insight into how the structural and electronic properties of the molecules mediate the hole/electron-transfer process.

2. Experimental Methods

2.1. Synthesis. Each of the thallium-containing compounds described herein was prepared as the Tl(III) complex with a chloride counterion.[28] The unlabeled monomer **Zn-SW-PE**[29] and the ^{13}C-labeled compounds **Zn*Zn-SW-PEP**[22] and **Zn*-SW-PE**[22] also were prepared previously. Abbreviated names employed previously for the compounds are listed in the Supporting Information.

2.2. Electrochemistry. The electrochemical measurements were performed using techniques and instrumentation previously described.[30] The samples were contained in a three-compartment cell equipped with a Pt wire working electrode, a Pt mesh counter electrode, and a Ag/Ag^+ (butyronitrile) reference electrode. The solvent was CH_2Cl_2 containing 0.1 M Bu_4NPF_6 as the supporting

(30) Yang, S. I.; Seth, J.; Strachan, J.-P.; Gentemann, S.; Kim, D.; Holten, D.; Lindsey, J. S.; Bocian, D. F. *J. Porphyrins Phthalocyanines* **1999**, *3*, 117–147.

Chart 2

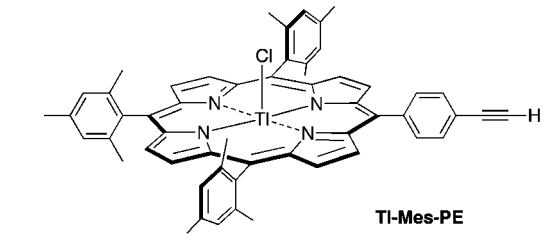

Tl-Mes-PE

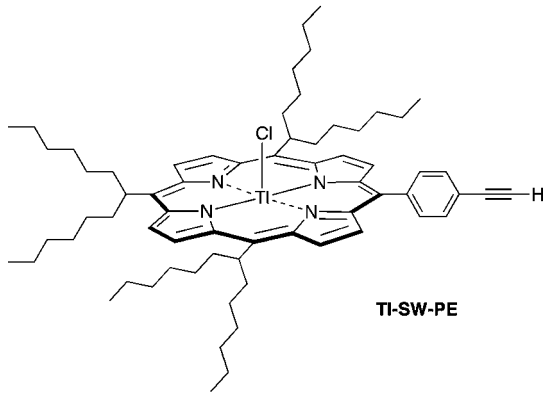

Tl-SW-PE

electrolyte. All reported potentials are with respect to ferrocene/ferrocenium = 0.19 V. The bulk oxidized complexes were prepared in a glovebox via quantitative coulometric bulk electrolysis at a Pt mesh electrode. The integrity of the samples was checked by cyclic voltammetry after the oxidation was completed. The samples were then transferred to an EPR tube and sealed in a glovebox.

2.3. EPR Spectroscopy and Simulations. The EPR spectra were recorded on an X-band spectrometer (Bruker EMX) equipped with an NMR gaussmeter and microwave frequency counter. The EPR spectra were obtained on samples that were typically 0.2 mM. The microwave power and magnetic field modulation amplitude were typically 5.7 mW and 0.32 G, respectively.

The EPR spectra of the monocations of the monomers were simulated with the WinSim program to obtain the values of the $^{203/205}$Tl and ^{14}N (and ^{13}C) hyperfine coupling constants and linewidths.[31] The EPR spectra of the monocations of the dyads were simulated with the ESR-EXN program.[32] The reader is referred to ref 32a for a detailed description of this program and its application to extract exchange rates from isotropic EPR spectra. The hyperfine coupling constants and line widths obtained from the simulations of the spectra of the monocations of the monomers were used as the initial values of these parameters in the simulations of the spectra of the monocations of the dyads. Prior to initiating the latter simulations, it was confirmed that the EPR spectra of the monocations of the monomers were faithfully reproduced by the ESR-EXN program using the parameters obtained from the WinSim program. The hole/electron-transfer rates at the different temperatures were derived from the simulations of the variable-temperature EPR spectra of the monocations of the dyads. The rate constants were adjusted manually to provide a best fit to the spectra as judged by the residuals between the observed and simulated spectra. Changes in the rate constants of ±10% from the best-fit values resulted in clearly poorer fits to the spectra. Finally, the hyperfine coupling constants and line widths vary somewhat with temperature (a few percent); consequently, these parameters were adjusted to optimize the fits of the EPR spectra obtained at the different temperatures.

2.4. Molecular Orbital Calculations. DFT calculations were performed with Spartan 08 for Windows (Wavefunction, Inc.) on a PC (Dell Optiplex GX270) equipped with a 3.2 GHz CPU and 3 GB of RAM.[33] The hybrid B3LYP functional and the LACVP basis set were employed. The equilibrium geometries were fully optimized using the default parameters of the Spartan 08 program.

3. Results

3.1. Redox Properties of the Thallium-Chelated Monomers and Dyads. The redox properties of the thallium-chelated monomers and dyads were examined prior to performing the EPR studies of the monocations of the various porphyrins. The oxidation potentials of the benchmark monomers, **Tl-SW-PE** and **Tl-Mes-PE**, are +0.75 and +0.86 V, respectively. The oxidation potentials of the swallowtail- and mesityl-substituted porphyrins in the various dyads are essentially identical to those of the respective monomers. The lower oxidation potential measured for **Tl-SW-PE** versus **Tl-Mes-PE** is consistent with the results of previous studies of zinc-chelated swallowtail- versus mesityl-substituted porphyrins.[29] Moreover, the oxidation potentials of the thallium-chelated porphyrins are substantially higher than those of the zinc chelates. In particular, the oxidation potential of each of the zinc-chelated swallowtail-substituted porphyrins examined herein (**Zn-SW-PE**, **Zn*-SW-PE**, and **Zn*Zn-SW-PEP**) is +0.43 V.

3.2. EPR Spectra of the Monocations of the Thallium-Chelated Monomers. The room-temperature EPR spectra of the monocations of **Tl-Mes-PE** and **Tl-SW-PE** are shown in Figure 1. For comparison, the room-temperature EPR spectra of the monocations of **Zn*-SW-PE** and **Zn-SW-PE** are also included in the figure. The EPR spectra of the thallium-chelated porphyrins exhibit a simple hyperfine doublet arising from coupling of the unpaired electron spin with the $I = 1/2$ thallium nuclei. No additional hyperfine structure is observed; such structure might have arisen due to resolving of the hyperfine doublets of the ^{203}Tl and ^{205}Tl nuclei or resolving of the nine-line pattern expected from the ^{14}N nuclei (cf. **Zn-SW-PE**). Consistent with early EPR studies of ^{205}Tl-chelated porphyrins,[27] the ^{203}Tl/^{205}Tl hyperfine couplings for the monocations of **Tl-SW-PE** and **Tl-Mes-PE** are substantial (16.7 and 24.9 G, respectively) and much larger than the ^{14}N and ^{13}C hyperfine couplings in **Zn-SW-PE** and/or **Zn*-SW-PE** (1.7 and 6.3 G, respectively).

3.3. EPR Spectra of the Monocations of the TlTl-Mes-PEP, TlTl-SW-PEP, TlTl-Mes-PEEP, and Zn*Zn-SW-PEP Dyads. The variable-temperature EPR spectra of the monocations of **TlTl-Mes-PEP**, **TlTl-SW-PEP**, and **TlTl-Mes-PEEP** are shown in the left panels of Figures 2, 3, and S1 (Supporting Information), respectively. In the case of **TlTl-Mes-PEP** and **TlTl-Mes-PEEP**, spectra are not shown at temperatures below 160 K because the solvent/electrolyte mixture freezes and the spectra change abruptly and become extremely broad. In the case of **TlTl-SW-PEP**, spectra are not shown for temperatures below 210 K because aggregation appears to occur.

The EPR spectra of the monocations of all three thallium-chelated dyads are qualitatively similar to one another. In particular, a three-line ^{203}Tl/^{205}Tl hyperfine pattern is observed at room temperature; as the temperature is lowered, the pattern gradually evolves into a two-line hyperfine pattern. This general feature of the EPR spectra is indicative of hole/electron transfer

(31) (a) Duling, D. R. *J. Magn. Reson. B* **1994**, *104*, 105–110. (b) http://www.niehs.nih.gov/research/resources/software/tools/index.cfm (accession date, 03/18/2010).

(32) (a) Heinzer, J. *Mol. Phys.* **1971**, *22*, 167–177. (b) Heinzer, J. *Quantum Chemistry Program Exchange* **1972**, No. 209.

(33) Except for molecular mechanics and semiempirical models, the calculation methods used in Spartan have been documented in the following: Shao, Y.; et al. *Phys. Chem. Chem. Phys.* **2006**, *8*, 3172–3191.

Chart 3

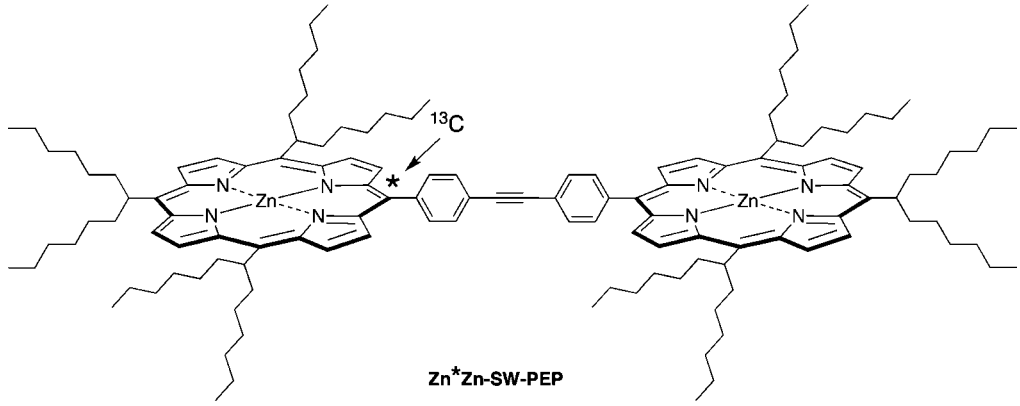

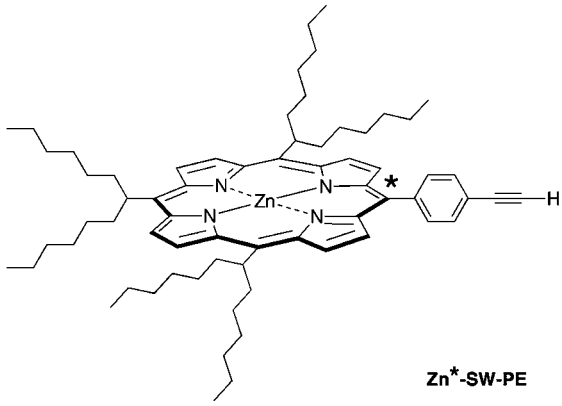

at room temperature that is relatively rapid on the EPR time scale defined by the ^{203}Tl/^{205}Tl hyperfine clock (swallowtail, 44.8 MHz; mesityl, 65.4 MHz) and slows down as the temperature is lowered.

Simulations of the variable-temperature EPR spectra of the monocations of **TlTl-Mes-PEP**, **TlTl-SW-PEP**, and **TlTl-Mes-PEEP** are shown in the right panels of Figures 2, 3, and S1 (Supporting Information), respectively. The hyperfine coupling constants and line widths used for all the simulations are compiled in Table S1 (Supporting Information). The hole/electron-transfer rates derived from the simulations are shown above each spectral trace. At room temperature, rates for **TlTl-Mes-PEP**, **TlTl-SW-PEP**, and **TlTl-Mes-PEEP** are 1.0×10^9, 4.9×10^8, and 5.1×10^8 s^{-1}, respectively. As the temperature is lowered, the rates decrease; however, at temperatures below 230 K, the decrease is more gradual. Similar behavior is observed in the variable-temperature EPR spectra of the

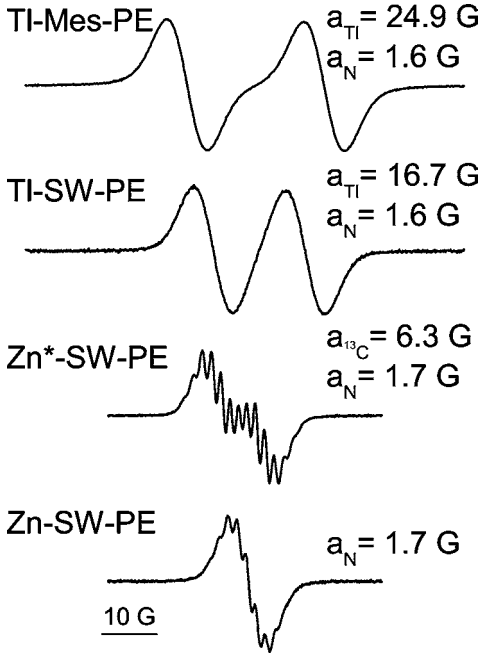

Figure 1. Room-temperature EPR spectra of the monocations of **Tl-Mes-PE**, **Tl-SW-PE**, **Zn*-SW-PE**, and **Zn-SW-PE**.

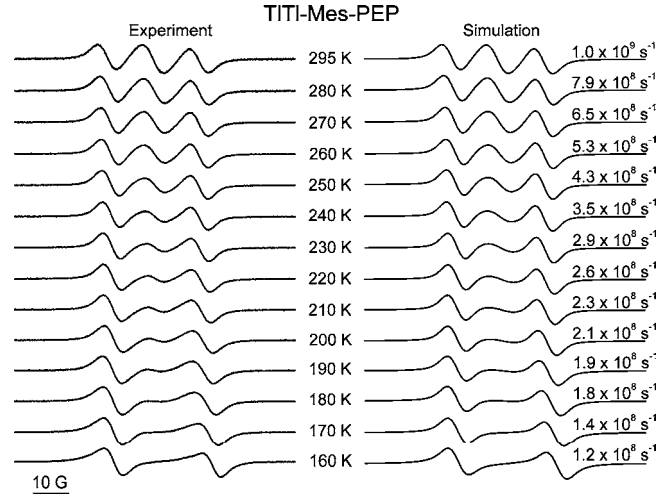

Figure 2. Variable-temperature EPR spectra of the monocation of **TlTl-Mes-PEP** (left panel) and simulated spectra (right panel) with derived hole/electron-transfer rates.

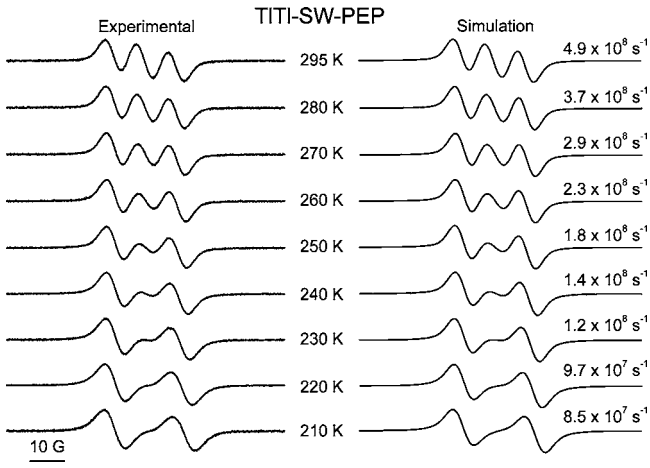

Figure 3. Variable-temperature EPR spectra of the monocation of **TlTl-SW-PEP** (left panel) and simulated spectra (right panel) with derived hole/electron-transfer rates.

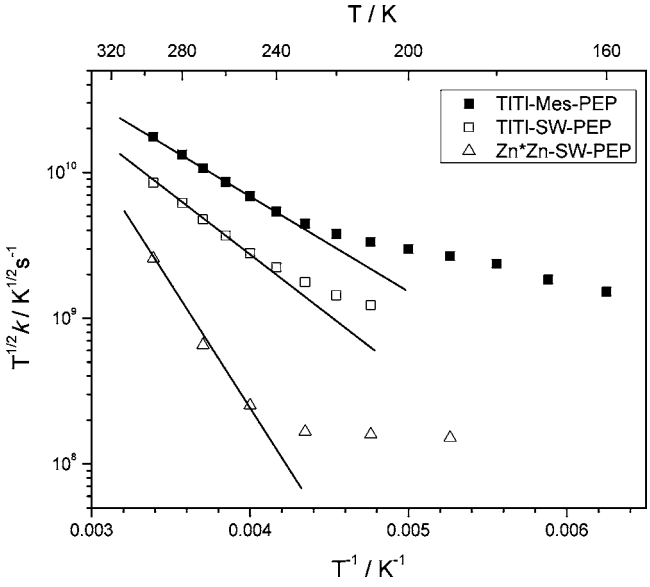

Figure 4. Marcus-equation plots for the monocations of **TlTl-Mes-PEP**, **TlTl-SW-PEP**, and **Zn*Zn-SW-PEP**.

monocation of **Zn*Zn-SW-PEP** (Figure S2, Supporting Information), which exhibits a room-temperature hole/electron-transfer rate of 1.5×10^8 s^{-1}. Accordingly, the rate for the zinc-chelated dyad is ~7-fold slower than that observed for the thallium-chelated analogue. However, it should be noted that the uncertainty in the rates derived from the spectral simulations for the monocation of **Zn*Zn-SW-PEP** is larger than that for the monocations of the three Tl dyads, owing to the much smaller hyperfine couplings of the unpaired electron to the ^{13}C and ^{14}N nuclei.

To probe further the temperature dependence of the hole/electron-transfer rates, the rates were plotted logarithmically versus $1/T$. Plots of $kT^{1/2}$ versus $1/T$ for the monocations of **TlTl-Mes-PEP**, **TlTl-SW-PEP**, and **Zn*Zn-SW-PEP** are shown in Figure 4. The data for the monocation of **TlTl-Mes-PEEP** are excluded from the figure for clarity; a plot for this dyad is shown in Figure S3 (Supporting Information). This approach assumes that hole/electron transfer can be modeled using the semiclassical Marcus equation[34] in the nonadiabatic limit,[35]

$$k = AT^{-1/2} \exp(-\Delta G^{\ddagger}/k_B T) \quad (1)$$

where $\Delta G^{\ddagger} = (\Delta G_o + \lambda)^2/4\lambda$, $A = (4\pi^3/h^2\lambda k_B)^{1/2}|V^2|$, ΔG_o is the free energy change associated with hole/electron transfer, λ is the reorganization energy, and V is the effective electronic coupling. Because the dyads studied herein are symmetrical, the hole/electron transfer in the monocations is an isoenergetic process, and $\Delta G_o = 0$.

Inspection of Figure 4 (and Figure S3, Supporting Information) shows that the data for all four dyads exhibit approximately biphasic behavior, with a break in the 230−250 K range. Above the break region, the data exhibit a positive slope; below the break region, the slope approaches zero. The data above the break region are fit reasonably well with eq 1. However, nearly equivalent fits are obtained using eq 1 in the adiabatic limit (no T dependence in the prefactor). The values for $\Delta G^{\ddagger}$ and A obtained from the slope and intercept of the linear fits to the data above the break region are summarized in Table 1. The data below the break region were not fit because $\Delta G^{\ddagger}$ is very small/negligible ($<k_B T$). The values of $\Delta G^{\ddagger}$ obtained (for data above 230−250 K) for the monocations of **TlTl-Mes-PEP**, **TlTl-SW-PEP**, and **TlTl-Mes-PEEP** are all similar to one another and relatively small (~12 kJ mol^{-1}). The value of $\Delta G^{\ddagger}$ obtained for the monocation of **Zn*Zn-SW-PEP** is somewhat larger (~33 kJ mol^{-1}). This value is less certain than that for the thallium chelates because of the larger uncertainty in the rates derived for the zinc chelate (Figure S2, Supporting Information).

3.4. EPR Spectra of the Monocations of the TlTl-Mes-Φ_n (n = 1−4) Dyads. The variable-temperature EPR spectra of the monocations of **TlTl-Mes-Φ_n** (n = 1−4) are shown in the left panels of Figures 5, S4, S5 (Supporting Information), and 6, respectively. For all four dyads, spectra are not shown at temperatures below 160 K because the solvent/electrolyte mixture freezes and the spectra change abruptly and become extremely broad.

The EPR spectra of the monocations of **TlTl-Mes-Φ_1** (Figure 5) and **TlTl-Mes-Φ_2** (Figure S4, Supporting Information) are qualitatively similar to one another and similar to those of the monocations of **TlTl-Mes-PEP**, **TlTl-SW-PEP**, and **TlTl-Mes-PEEP**. In particular, the spectra of the monocations of **TlTl-Mes-Φ_1** and **TlTl-Mes-Φ_2** both exhibit a three-line ^{203}Tl/^{205}Tl hyperfine pattern at room temperature, which gradually evolves into a two-line hyperfine pattern as the temperature is lowered. The EPR spectra of the monocations of **TlTl-Mes-Φ_3** (Figure S5, Supporting Information) and **TlTl-Mes-Φ_4** (Figure 6) are different in that a three-line ^{203}Tl/^{205}Tl hyperfine pattern is observed at all temperatures above 160 K.

Simulations of the variable-temperature EPR spectra of the monocations of **TlTl-Mes-Φ_n** (n = 1−4) are shown in the right panels of Figures 5, S4, S5 (Supporting Information), and 6, respectively. The hyperfine coupling constants and line widths used for all the simulations are compiled in Table S2 (Supporting Information). The hole/electron-transfer rates derived from the simulations are shown above each spectral trace. At room temperature, the hole/electron-transfer rates for **TlTl-Mes-Φ_n** (n = 1−4) are >3.9×10^9, 1.9×10^9, 9.2×10^8, and 5.8×10^8 s^{-1}, respectively. The hole/electron-transfer rate for **TlTl-Mes-**

(34) Marcus, R. A.; Sutin, N. *Biochim. Biophys. Acta* **1985**, *811*, 265–322.
(35) Nitzan, A. *Chemical Dynamics in Condensed Phases: Relaxation, Transfer, and Reactions in Condensed Molecular Systems*; Oxford University Press: New York, 2006.

Table 1. Activation Energies ($\Delta G^{\ddagger}$) and Prefactors (A) for the Hole-Transfer Process Determined from Fits of the Higher-Temperature Kinetic Data

Dyad	$\Delta G^{\ddagger}$ (kJ mol^{-1})	A ($T^{1/2}$, s^{-1})
TlTl-Mes-PEP	12.5	3.0×10^{12}
TlTl-SW-PEP	11.7	8.9×10^{11}
Zn*Zn-SW-PEP	32.6	9.8×10^{14}
TlTl-Mes-PEEP	11.7	1.4×10^{12}
TlTl-Mes-Φ_1	12.5	1.8×10^{13}
TlTl-Mes-Φ_2	15.0	1.6×10^{13}
TlTl-Mes-Φ_3	8.4[a]	4.8×10^{11} [a]
TlTl-Mes-Φ_4	*b*	*b*

[a] Determined from the data above 260 K. [b] The activation energy is very small/negligible ($<k_BT$) (see text).

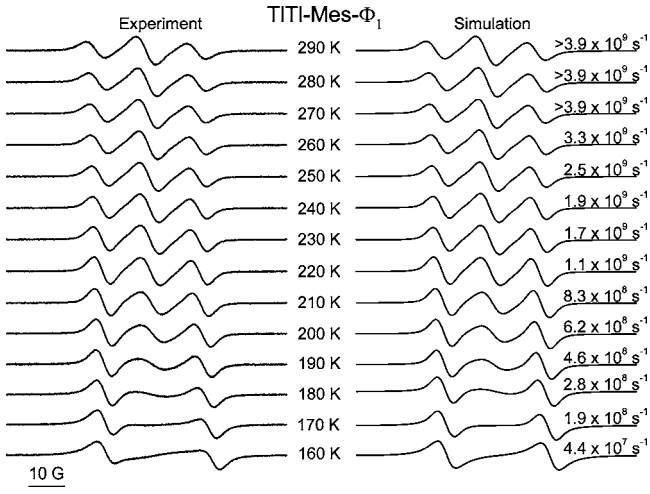

Figure 5. Variable-temperature EPR spectra of the monocation of **TlTl-Mes-Φ_1** (left panel) and simulated spectra (right panel) with derived hole/electron-transfer rates.

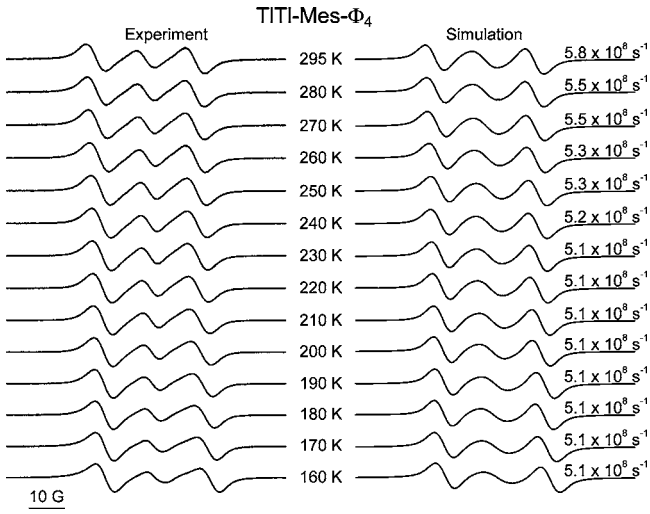

Figure 6. Variable-temperature EPR spectra of the monocation of **TlTl-Mes-Φ_4** (left panel) and simulated spectra (right panel) with derived hole/electron-transfer rates.

Φ_1 appears to be at the upper limit for measurements using the ^{203}Tl/^{205}Tl hyperfine clock, in that the spectra do not change appreciably above 270 K. The simulations further indicate that the decrease in rate as the temperature is lowered becomes less pronounced as the number of phenylene units in the linker increases. Indeed, for the monocation of **TlTl-Mes-Φ_4**, the hole/electron-transfer rate does not change appreciably over the 160−295 K temperature range.

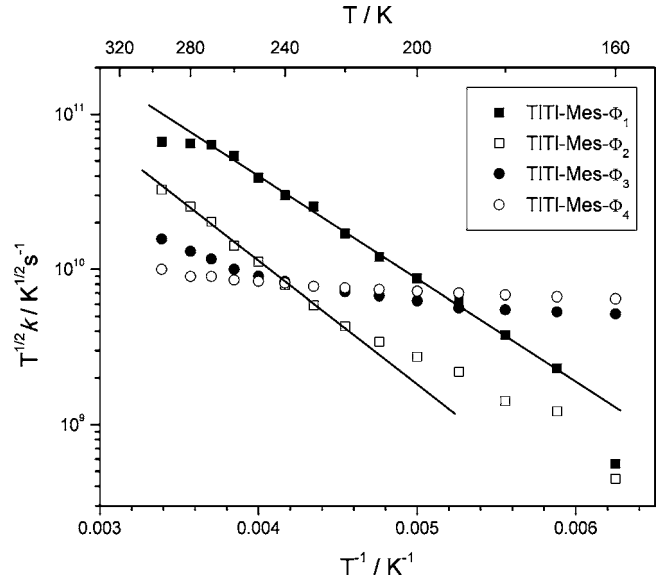

Figure 7. Marcus-equation plots for the monocations of **TlTl-Mes-Φ_n** ($n = 1-4$).

Logarithmic plots of $kT^{1/2}$ versus $1/T$ for the monocations of **TlTl-Mes-Φ_n** ($n = 1-4$) are shown in Figure 7. The key features of the plots for the four dyads are as follows.

(1) The plot for the monocation of **TlTl-Mes-Φ_1** exhibits a positive slope over the 160−270 K temperature range, and there is no indication of biphasic behavior. The data in the 170−270 K temperature range are well fit with eq 1 (or the adiabatic equivalent) and yield a $\Delta G^{\ddagger}$ of 12.5 kJ mol^{-1}, similar to those for **TlTl-Mes-PEP** and **TlTl-SW-PEEP**. The two highest temperature points (280 and 295 K) fall off the line owing to the fact that the hole/electron-transfer rate is beyond the limit of the ^{203}Tl/^{205}Tl hyperfine clock. The lowest-temperature point also falls off the line.

(2) The plot for the monocation of **TlTl-Mes-Φ_2** differs somewhat from that of **TlTl-Mes-Φ_1** in that a break in slope begins to appear near 200 K, and below that temperature the data begin to flatten (the slope tends toward zero). The data above 220 K are well fit with eq 1 (or the adiabatic equivalent) and yield a $\Delta G^{\ddagger}$ of 15.0 kJ mol^{-1}, again similar to those for **TlTl-Mes-Φ_1**, **TlTl-Mes-PEP**, and **TlTl-SW-PEEP**. The data below 200 K were not fit.

(3) The temperature dependence for the monocation of **TlTl-Mes-Φ_3** is much weaker than that for **TlTl-Mes-Φ_1** or **TlTl-Mes-Φ_2** and exhibits only a slight upturn in slope above 260 K. Fits to these data (not shown) predict a value for $\Delta G^{\ddagger}$ of 8.4 kJ mol^{-1} (Table 1), which is somewhat smaller than those for the other dyads. However, this value is much less certain owing to the limited number of data points.

(4) The plot for the monocation of **TlTl-Mes-Φ_4** is essentially flat over the 160−295 K temperature range; thus, the $\Delta G^{\ddagger}$ value is very small/negligible ($<k_BT$).

3.5. Molecular Orbital Characteristics of the Porphyrins and Linkers. To gain additional insight into the relative energies of the molecular orbitals of the porphyrins and linkers in the various dyads, DFT calculations were performed on a series of model compounds. The focus of these calculations was the relative energies of the HOMOs of the molecules, which are the key orbitals for the hole/electron-transfer process. The

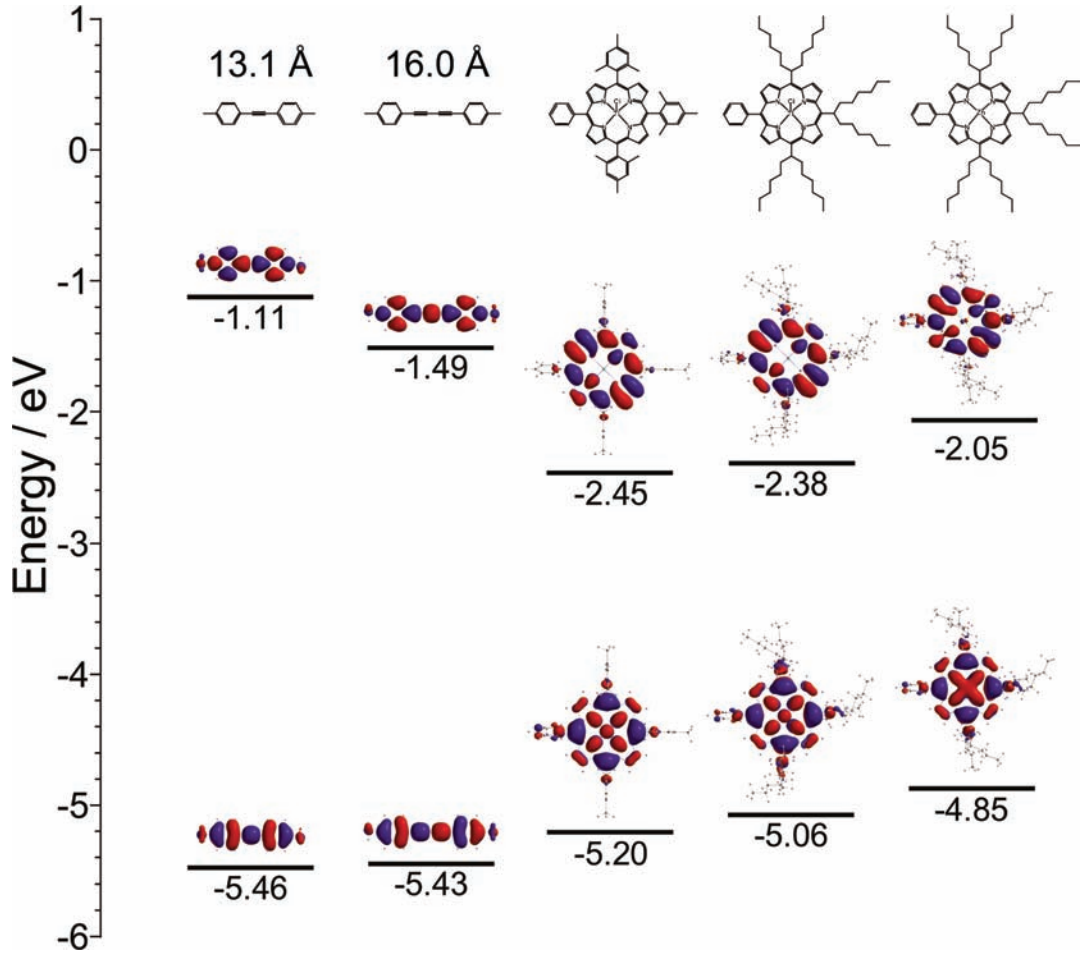

Figure 8. Calculated electron densities and energies for the HOMOs and LUMOs of **PEP**, **PEEP**, **Tl-Mes-P**, **Tl-SW-P**, and **Zn-SW-P**. The linker length is included above each structure.

porphyrin model compounds included thallium- and zinc-chelated swallowtail-substituted monomers with one meso phenyl substituent (**Tl-SW-P** and **Zn-SW-P**) and a thallium-chelated mesityl-substituted monomer with one meso phenyl substituent (**Tl-Mes-P**). The linker model compounds included diarylethyne (**PEP**), diphenylbutadiyne (**PEEP**), and monophenylene through quaterphenylene ($\mathbf{\Phi}_n$, $n = 1-4$). For the DFT calculations of these model compounds, the linking positions were terminated with methyl groups.

The calculated electron densities and energies for the HOMOs and lowest unoccupied molecular orbitals (LUMOs) of **PEP**, **PEEP**, **Tl-Mes-P**, **Tl-SW-P**, and **Zn-SW-P** are shown in Figure 8. The structures of the molecules are included in the figure; the length of each linker (i.e., the edge-to-edge distance between the porphyrins in dyads employing the linker) is included above the structures for those model compounds. The calculations predict that the HOMO energies for the porphyrins increase along the series **Tl-Mes-P** (−5.20 eV), **Tl-SW-P** (−5.06 eV), and **Zn-SW-P** (−4.85 eV). This trend parallels that observed for the oxidation potentials of the benchmark porphyrins **Tl-Mes-PE** (+0.86 V), **Tl-SW-PE** (+0.75 V), and **Zn-SW-PE** (+0.43 V). [Note that a lower oxidation potential implies a higher (less negative) HOMO energy; i.e., the molecule is easier to oxidize.] The calculations further predict that the HOMO energies for **PEP** (−5.43 eV) and **PEEP** (−5.46 eV) are similar to one another and fall below those of the porphyrins. The actual energy difference between the HOMO of the porphyrin and the HOMO of the linker is likely larger than the calculated difference, in that electrochemical studies provide no evidence for linker oxidation out to potentials of +1.5 V.

The calculated electron densities and energies for the HOMOs and LUMOs of $\mathbf{\Phi}_n$ ($n = 1-4$) and **Tl-Mes-P** are shown in Figure 9. The structures of the molecules are included in the figure; the length of each linker is included above the structures for those model compounds. The calculations predict that the HOMO energies for all four oligo(*p*-phenylene) linkers, $\mathbf{\Phi_1}$ (−6.14 eV), $\mathbf{\Phi_2}$ (−5.74 eV), $\mathbf{\Phi_3}$ (−5.57 eV), and $\mathbf{\Phi_4}$ (−5.51 eV), fall below those of **Tl-Mes-P** (−5.20 eV) and increase monotonically as the number of phenylene units increases. Here again, the actual energy difference between the HOMOs of the porphyrin and linkers is likely larger than the calculated difference, in that electrochemical studies provide no evidence for linker oxidation out to potentials of +1.5 V.

4. Discussion

In this study, we have examined the effects of porphyrin and linker characteristics on the hole/electron-transfer rate in a series of singly oxidized thallium-chelated porphyrin dyads wherein the thallium nuclei serve as a hyperfine clock. In the sections below, we first discuss some general characteristics of the hole/electron-transfer process. We then turn to more specific effects that result from changing the type of porphyrin or linker in the dyad.

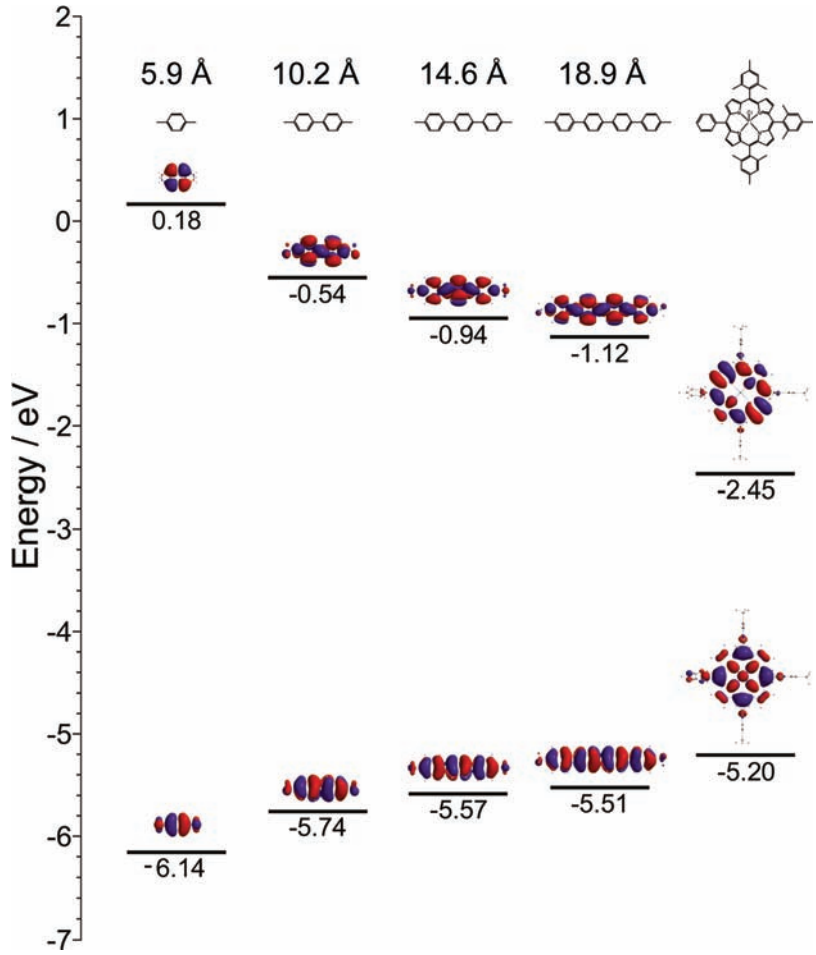

Figure 9. Calculated electron densities and energies for the HOMOs and LUMOs of Φ_n ($n = 1-4$) and **Tl-Mes-P**. The linker length is included above each structure.

4.1. General Characteristics of the Hole/Electron-Transfer Process. The key general observations from the studies of the hole/electron-transfer process in the monocations of the thallium-chelated porphyrin dyads are as follows.

(1) Hole/electron-transfer at room temperature occurs at rates that correspond to time scales in the hundreds of picoseconds to sub-10 ns regime. These rates are significantly faster than can be easily determined using ^{14}N, ^{1}H, or ^{13}C hyperfine clocks.[13,18,19,22,23,36,37] More importantly, the time scales for hole/electron transfer determined via the EPR studies of the thallium-chelated porphyrins are in good general agreement with those extracted from time-resolved optical studies of similar processes in oxidized porphyrin arrays.[17b,c] These latter studies are more difficult to perform than the relatively straightforward EPR studies reported herein.

(2) The hole/electron-transfer process is weakly activated at room temperature (and somewhat below) and becomes essentially activationless at lower temperatures (Figures 4, 7, and S3, Supporting Information). The exceptions are **TlTl-Mes-Φ_4**, which exhibits essentially activationless hole/electron transfer at all temperatures, and **TlTl-Mes-Φ_1**, which exhibits a weakly activated hole/electron transfer at all temperatures (Figure 7). The weak/negligible activation energies for the hole/electron transfer in the monocations of the porphyrin dyads are consistent with a linker-mediated superexchange (tunneling) mechanism. In the superexchange-mediated process, the linker orbitals are not populated and do not serve as discrete intermediates during the charge-transfer event. This mechanism can be contrasted with a hopping process wherein the linker orbitals are populated during the charge-transfer event. Hopping processes have typically been associated with temperature-dependent rates. However, Wasielewski, Ratner, and co-workers have recently pointed out that temperature-dependent rates do not preclude a tunneling mechanism.[38] Regardless, a hopping mechanism would not be anticipated for the hole/electron-transfer process in the monocations of the porphyrin dyads, owing to the significant energy difference between the porphyrin and linker HOMOs (Figures 8 and 9).

(3) The hole/electron-transfer process in the weakly activated region can be modeled equally well using semiclassical Marcus theory in either the nonadiabatic or adiabatic limit. In the nonadiabatic limit, the electronic motion is slower than the vibrational motion and the prefactor reflects the tunneling frequency, which is a function of the electronic coupling. In the adiabatic limit, the electronic motions are faster than the vibrational motions and the prefactor reflects the effective

(36) Lancaster, K.; Odom, S. A.; Jones, S. C.; Thayumanavan, S.; Marder, S. R.; Bredas, J.-L.; Coropceanu, V.; Barlow, S. *J. Am. Chem. Soc.* **2009**, *131*, 1717–1723.
(37) Wilson, T. M.; Hori, T.; Yoon, M.-C.; Aratani, N.; Osuka, A.; Kim, D.; Wasielewski, M. R. *J. Am. Chem. Soc.* **2010**, *132*, 1383–1388.
(38) Goldsmith, R. H.; DeLeon, O.; Wilson, T. M.; Finkelstein-Shapiro, D.; Ratner, M. A.; Wasielewski, M. R. *J. Phys. Chem. A* **2008**, *112*, 4410–4414.

frequency of nuclear motions that govern barrier crossing; the most important nuclear motions are generally the collective, relatively slow motions of the solvent.[39] The frequencies of the solvent motions are typically in the $10^{11}-10^{12}$ s^{-1} range.[40,41] These values are similar to the prefactors ($AT^{-1/2}$) measured for all the thallium-chelated porphyrin dyads ($AT^{-1/2}$ for the zinc chelate is somewhat larger; see Table 1). This characteristic of the hole/electron-transfer process, along with the fact that it can be modeled equally well using either the nonadiabatic or adiabatic approach, suggests that hole/electron transfer occurs in a region that is intermediate between the two limits.

4.2. Effects of Porphyrin and Linker Characteristics on the Hole/Electron-Transfer Process. The characteristics of the hole/electron-transfer process vary depending on the type of porphyrin and/or linker. This is clearly evident in the rate versus temperature plots shown in Figures 4, S3 (Supporting Information), and 7. In the case of the **PEP**-linked dyads, the hole/electron-transfer rates decrease (Figure 4) along the series **TlTl-Mes-PEP** > **TlTl-SW-PEP** > **Zn*Zn-SW-PEP**. This trend is opposite to that for the energy difference between the HOMOs of the porphyrin and linker, which increases along the series **TlTl-Mes-PEP** < **TlTl-SW-PEP** < **Zn*Zn-SW-PEP** (Figure 8). This trend in the hole/electron-transfer rates is maintained in both the weakly activated and activationless regions (Figure 4). The trend is also exhibited for the diphenylbutadiyne-linked dyad (Figure S3, Supporting Information). In the case of the $\mathbf{\Phi}_n$-linked dyads, the temperature dependence is more complex. At room temperature, the hole/electron-transfer rates decrease as the number of phenylene units increases. However, owing to differences in activation behavior, the rates for **TlTl-Mes-Φ_3** and **TlTl-Mes-Φ_4** cross over those for **TlTl-Mes-Φ_1** and **TlTl-Mes-Φ_2** as the temperature is lowered (Figure 7). Thus, at low temperatures, the dyads with longer linkers exhibit faster rates than those with shorter linkers. Below, we examine how the porphyrin and linker HOMO energies, linker length, and linker torsional motions affect the hole/electron-transfer process.

4.2.1. Effects of Porphyrin and Linker HOMO Energies and Linker Length. The **PEP**-linked porphyrin dyads serve as a platform for examining the effects of altering the porphyrin HOMO energy in the absence of changes in either linker HOMO energy or linker length. We consider the **PEEP**-linked dyad in this same series owing to the fact that the linker HOMO energy is predicted to be nearly the same as that of **PEP** and the linker length is only slightly longer (Figure 8). In the case of the $\mathbf{\Phi}_n$-linked dyads, the porphyrin HOMO energy is constant; however, both the linker HOMO energy and linker length vary as the number of phenylene units increases (Figure 9).

The hole/electron-transfer rate is related to the transmission coefficient through the tunneling barrier scaled by the activation energy.[42] The transmission coefficient, in turn, depends exponentially on both the height and width of the barrier.[43] The height of the barrier for the hole/electron-tunneling process would be expected to be related to the porphyrin−linker HOMO energy difference, ΔE_{PL}. The width of the barrier would be expected to be related to the length of the linker, L_{link}. In a simple approximation wherein one assumes a high and/or wide rectangular tunneling barrier, the transmission coefficient, T, is related to the effective barrier, B_{eff}, by

$$T \propto \exp(-B_{eff}) \qquad (2)$$

where $B_{eff} = (\Delta E_{PL})^{1/2} L_{link}$.

Table 2. Room-Temperature Hole-Transfer Rates, Porphyrin−Linker HOMO Energy Differences (ΔE_{PL}), Linker Lengths (L_{link}), and Effective Barriers (B_{eff})

dyad	k (s^{-1})	ΔE_{PL} (eV)	L_{link} (Å)	B_{eff}[a] ($eV^{1/2}\cdot$Å)
TlTl-Mes-PEP	1.0×10^9	0.26	13.1	6.7
TlTl-SW-PEP	4.9×10^8	0.40	13.1	8.3
Zn*Zn-SW-PEP	1.5×10^8	0.61	13.1	10.2
TlTl-Mes-PEEP	5.1×10^8	0.23	16.0	7.7
TlTl-Mes-Φ_1	$>3.9 \times 10^9$	0.96	5.9	5.8
TlTl-Mes-Φ_2	1.9×10^9	0.56	10.2	7.6
TlTl-Mes-Φ_3	9.2×10^8	0.37	14.6	8.9
TlTl-Mes-Φ_4	5.8×10^8	0.31	18.9	10.5

[a] $B_{eff} = (\Delta E_{PL})^{1/2} L_{link}$

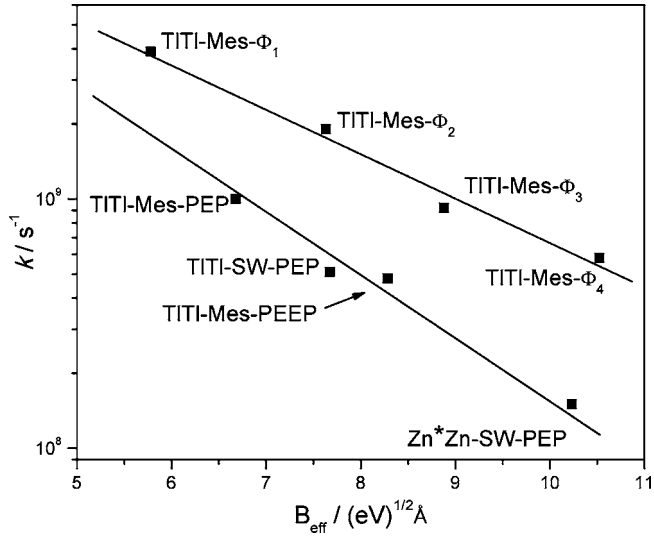

Figure 10. Room-temperature hole/electron-transfer rate versus effective barrier.

The room-temperature hole/electron-transfer rates for the monocations of the **PEP**- and **PEEP**-linked dyads are compiled in Table 2, along with the values of ΔE_{PL}, L_{link}, and B_{eff}. Logarithmic plots of the rate versus B_{eff} for the four dyads are shown in Figure 10. As can be seen, the data exhibit an approximately linear dependence, consistent with the simple model. The fact that the data for the monocation of **Zn*Zn-Mes-PEP** fit the trend is somewhat unexpected, given that the $\Delta G^{\ddagger}$ value for this dyad is different from those for the thallium-chelated dyads. At lower temperatures, in the activationless region, there are insufficient data to explore the applicability of the model.

The success of the rectangular-barrier model for the **PEP**- and **PEEP**-linked dyads prompted us to apply the model to the $\mathbf{\Phi}_n$-linked dyads. The room-temperature rates and ΔE_{PL}, L_{link}, and B_{eff} values for these dyads are included in Table 2; logarithmic plots of the rate versus B_{eff} are shown in Figure 10. Surprisingly, the data again exhibit a linear dependence, consistent with the simple model. Clearly the model cannot work in the low-temperature region, owing to the fact that the rates of the mono- and di-*p*-phenylene-linked dyads cross over those of the tri- and tetra-*p*-phenylene-linked dyads.

The fact that the hole/electron-transfer process for all the dyads (at room temperature) can be accounted for by a simple

(39) Demadis, K. D.; Hartshorn, C. M.; Meyer, T. J. *Chem. Rev.* **2001**, *101*, 2655–2685.
(40) Sutin, N. *Prog. Inorg. Chem.* **1983**, *30*, 441–498.
(41) Horng, J. L.; Gardecki, J. A.; Papazyan, A.; Maroncelli, M. *J. Phys. Chem.* **1995**, *99*, 17311–17337.
(42) Eyring, H. *Rev. Mod. Phys.* **1962**, *34*, 616–610.
(43) Merzbacher, E. *Quantum Mechanics*, 2nd ed.; Wiley: New York, 1970.

model involving transmission through a rectangular barrier suggests that the finer details of the electronic structure of the porphyrin and linker are not paramount in determining the rates. This view is consistent with the fact that the range of hole/electron-transfer rates is relatively narrow, despite the fairly significant changes in the nature of the porphyrin (zinc versus thallium; swallowtail versus mesityl) and linker. Nevertheless, additional factors appear to influence the rates at low temperatures. Possibly, the solvent comes into play as the temperature is lowered and the mobility of the solvent/electrolyte decreases.

4.2.2. Effects of Linker Torsional Motions. A question that remains concerns the nature of the process that gives rise to the weak activation of hole/electron transfer. In Marcus theory in the nonadiabatic limit (eq 1), the reorganization energy would dictate the activation free energy, in particular, $\Delta G^{\ddagger} = \lambda/4$ (because $\Delta G_o = 0$). Accordingly, the $\Delta G^{\ddagger}$ values determined for the monocations of the thallium-chelated porphyrin dyads would suggest λ values of 0.5−0.6 eV (~1.3 eV for the zinc chelate). These values are generally smaller than those expected for outer-sphere (solvent) reorganization energies of the pure solvent (~1.5 eV),[17] which will be altered by the presence of the electrolyte. Additionally, the λ values noted above are larger than the inner-sphere (molecular) reorganization energies associated with formation of π-cation radicals of tetrapyrroles (0.1−0.2 eV).[44] Furthermore, if inner-sphere reorganization were dictating the $\Delta G^{\ddagger}$ value, then all the thallium chelates might be expected to exhibit weakly activated hole/electron transfer at higher temperatures. In fact, activated transfer is not observed for the monocation of **TlTl-Mes-Φ_4** (and only very weakly so for **TlTl-Mes-Φ_3**). Collectively, these considerations suggest that other factors must contribute substantially to the activation energy (and thus to the reorganization energy) for hole/electron transfer in the dyads.

The most self-consistent explanation for the weakly activated hole/electron transfer is that torsional motions of the phenyl rings in the linker contribute to the process. In particular, rotation of the phenyl rings toward coplanarity with the porphyrin would be expected to enhance the hole/electron transfer via the increase of a conjugative pathway. In this regard, our previous optical studies of hole/electron in oxidized porphyrin arrays have shown that the presence of ortho-dimethyl groups on the phenyl rings of **PEP** linkers slows the hole/electron-transfer process.[17] The decreased rate is attributed to the fact that the ortho-dimethyl groups substantially increase the torsional barrier for phenyl-ring rotation.[45] The contribution of torsional motions could explain why the activation energies for all the thallium-chelated dyads with **PEP** (and **PEEP**) linkers are similar and why the successive addition of phenylene rings to the linker moves the hole/electron-transfer process from a weakly activated to an activationless region. In particular, the addition of each phenylene ring introduces another barrier to mutual coplanarity. For the **Φ_3** and **Φ_4** linkers, the barrier to mutual coplanarity would become so high as to preclude any type of torsional activation of the hole/electron-transfer process. The contribution of torsional motions to the activation energy could also explain why the energies for all the thallium chelates are lower than that for the zinc chelate (Table 1). In particular, previous studies have shown that distortions of porphyrins from planarity result in a lower phenyl-ring torsional barrier.[46] In this regard, crystallographic studies have shown that five-coordinate Tl(III) porphyrins are highly domed; in contrast, four-coordinate Zn(II) porphyrins are planar.[47]

Finally, it should be noted that the $\Delta G^{\ddagger}$ values determined for all the porphyrin dyads are much smaller than the measured aryl-ring torsional barriers in meso-substituted porphyrins. These barriers are in the 60−100 kJ mol^{-1} range.[45] Thus, any type of torsional motion that might contribute to activation of the hole/electron-transfer process in the monocations of the porphyrin dyads would necessarily involve only restricted rotation of the phenyl ring toward coplanarity with the porphyrin. In particular, the faster rates at higher temperature are due to an increase in the amplitude of the low-frequency, large-amplitude torsional motions that occurs upon population of higher vibrational states in the torsional potential energy well.

5. Summary and Outlook

The studies reported herein demonstrate that ^{203}Tl/^{205}Tl hyperfine interactions make excellent clocks for determining the hole/electron-transfer rates in the mono-π-cations of porphyrin dyads. In the case the diphenylethyne-, diphenylbutadiyne-, and phenylene-linked dyads, the time constants are in the hundreds of picoseconds to sub-10 ns regime, depending on the specific linker. These values are consistent with those recently determined using more elaborate optical techniques.[17] The studies further demonstrate that the hole/electron-transfer process is at best weakly activated at room temperature and somewhat below. At lower temperatures, the process is essentially activationless. The weak activation is attributed to restricted torsional motions of the phenyl rings of the linker.

The findings herein concerning hole/electron transfer have a number of implications. (1) Arrays of porphyrins can be designed in a rational manner to give ground-state hole/electron transfer in conjunction with an excited-state charge-separation unit. The ability to achieve hole/electron transfer over a long distance is an essential feature of an efficient charge-separation scheme. (2) Long linkers can be envisaged that still afford rapid rates of hole/electron transfer. A key feature of the design consideration is the energy gap between the HOMO of the porphyrin and the HOMO of the linker. (3) The above concepts could be implemented to design architectures wherein efficient hole/electron transfer is maintained while suppressing processes such as through-space excited-state energy transfer. The ability to control such processes may be especially important in arrays of hydroporphyrins, wherein through-space energy-transfer processes are quite facile.

The elucidation of the rates and mechanisms for hole/electron transfer in the monocations of the porphyrin dyads using ^{203}Tl/^{205}Tl hyperfine clocks suggests that this approach will be useful for probing hole/electron transfer in dyads of other types of tetrapyrroles, such as chlorins and bacteriochlorins. More generally, the ^{203}Tl/^{205}Tl hyperfine clocks should be useful for examining hole/electron transfer in a variety of coordination compounds, although the tetrapyrroles likely constitute a particularly attractive class of molecular architectures. In

(44) Felton, R. H. In *The Porphyrins*; Dolphin, D., Ed.; Academic Press: New York, 1978; Vol. 5, pp 53−178.
(45) (a) Eaton, S. S.; Eaton, G. R. *J. Am. Chem. Soc.* **1975**, *97*, 3660–3666. (b) Eaton, S. S.; Eaton, G. R. *J. Am. Chem. Soc.* **1977**, *99*, 6594–6599.
(46) Eaton, S. S.; Fishwald, D. M.; Eaton, G. R. *Inorg. Chem.* **1978**, *17*, 1542–1545.
(47) (a) Scheidt, W. R. In *The Porphyrins*; Dolphin, D., Ed.; Academic Press: New York, 1978; Vol. 3, pp 463−511. (b) Meyer, E. F., Jr.; Cullen, D. L. In *The Porphyrins*; Dolphin, D., Ed.; Academic Press: New York, 1978; Vol. 3, pp 512−529.

particular, the $^{203}Tl/^{205}Tl$ hyperfine clocks should be ideally suited for probing hole/electron transfer in larger arrays of tetrapyrroles. In such arrays, rapid hole/electron transfer over multiple sites further collapses the hyperfine structure,[18,19,37] additionally compromising the utility of ^{14}N and ^{1}H (or ^{13}C) hyperfine interactions as monitors of hole/electron transfer. Currently, we are in the process of preparing a series of other porphyrin, chlorin, and bacteriochlorin arrays for studies of hole/electron transfer. The elucidation of the hole/electron-transfer characteristics of all these various arrays will provide a foundation for incorporation of such architectures into solar-energy conversion systems.

Acknowledgment. This research was supported by grants from the Division of Chemical Sciences, Geosciences and Biosciences Division, Office of Basic Energy Sciences, Office of Science, U.S. Department of Energy, to D.F.B. (DE-FG02-05ER15660), J.S.L. (DE-FG02-96ER14632), and D.H. (DE-FG02-05ER15661).

Supporting Information Available: Abbreviated names employed previously for the compounds; complete ref 33; variable-temperature EPR spectra and simulated spectra with derived hole-transfer rates for **TlTl-Mes-PEEP**, **Zn*Zn-SW-PEP**, **TlTl-Mes-Φ_2**, and **TlTl-Mes-Φ_3**; EPR simulation parameters for all dyads; Marcus equation plots for **TlTl-Mes-PEEP**. This material is available free of charge via the Internet at http://pubs.acs.org.

JA105082D